Yang *et al. Energy Mater.* **2025**, *5*, 500006
DOI: 10.20517/energymater.2024.45

Energy Materials

Article

Open Access

Check for updates

Flexible, highly conductive, and microscopically disordered MXene film electrode constructed via *in-situ* carbon dots intercalation toward high-performance supercapacitors

Deyu Yang[1,#], Haonan Cui[1,#], Razium Ali Soomro[1], Peng Zhang[1,2,*], Bin Xu[1,3,*]

[1]State Key Laboratory of Organic-Inorganic Composites, Beijing Key Laboratory of Electrochemical Process and Technology for Materials, Beijing University of Chemical Technology, Beijing 100029, China.
[2]Henan Key Laboratory of Quantum Materials and Quantum Energy, School of Quantum Information Future Technology, Henan University, Zhengzhou 450046, Henan, China.
[3]Shaanxi Key Laboratory of Chemical Reaction Engineering, School of Chemistry and Chemical Engineering, Yan'an University, Yan'an 716000, Shaanxi, China.
[#]Authors contributed equally.

***Correspondence to:** Dr. Peng Zhang, Henan Key Laboratory of Quantum Materials and Quantum Energy, School of Quantum Information Future Technology, Henan University, Mingli Street, Zhengzhou 450046, Henan, China. E-mail: pengzhang@henu.edu.cn; Prof. Bin Xu, State Key Laboratory of Organic-Inorganic Composites, Beijing Key Laboratory of Electrochemical Process and Technology for Materials, Beijing University of Chemical Technology, 15 Beisanhuan East Road, Chaoyang District, Beijing 100029, China; Shaanxi Key Laboratory of Chemical Reaction Engineering, School of Chemistry and Chemical Engineering, Yan'an University, 580 Shengdi Road, Yan'an 716000, Shaanxi, China. E-mail: xubin@yau.edu.cn/xubin@mail.buct.edu.cn

How to cite this article: Yang, D.; Cui, H.; Soomro, R. A.; Zhang, P.; Xu, B. Flexible, highly conductive, and microscopically disordered MXene film electrode constructed via *in-situ* carbon dots intercalation toward high-performance supercapacitors. *Energy Mater.* **2025**, *5*, 500006. https://dx.doi.org/10.20517/energymater.2024.45

Received: 11 May 2024 **First Decision:** 4 Jun 2024 **Revised:** 9 Jul 2024 **Accepted:** 22 Aug 2024 **Published:** 6 Jan 2025

Academic Editors: Yuping Wu, Sining Yun **Copy Editor:** Fangling Lan **Production Editor:** Fangling Lan

Abstract

Two-dimensional MXenes are being recognized as favorable supercapacitor electrode materials due to their metallic conductivity, excellent hydrophilicity, high density, and rich surface chemistry. However, layer-restacking within MXene electrodes substantially hinders the efficient utilization of the active surface and ion accessibility. Herein, a unique carbon dots (CDs) intercalated MXene film (CDs-MF) is designed by introducing gelatin within the MXene interlayers followed by carbonization. The CD intercalation can enlarge the interlayer spacing of MXene film and induce microscopic disorder, exposing the active surface and facilitating ion diffusion within the electrode. The optimal CDs-MF electrode shows exceptional capacitive performance, achieving high gravimetric/volumetric

capacitances (396.4 F g^{-1} at 1 A g^{-1} and 1,153.2 F cm^{-3} at 1 A cm^{-3}), superior rate capability (123.2 F g^{-1} at 1,000 A g^{-1}), and excellent cycling stability with no capacitance decay over 100,000 cycles. Moreover, the assembled quasi-solid-state symmetric supercapacitor exhibited a maximum energy density of 21.2 Wh L^{-1} and a power density of 12 kW L^{-1}. The device could operate efficiently under various configurations (series or parallel) and different bending angles, reflecting its promising application in flexible energy storage devices.

Keywords: Supercapacitors, carbon dots intercalation, MXene, flexible film, electrochemical performance

INTRODUCTION

Supercapacitors are efficient energy storage systems owing to their extended cycle lifespan, rapid charge-discharge rate, and high power output[1,2]. They are categorized as either electric double-layer capacitors (EDLC) or pseudocapacitors according to their charge-storage mechanism[3]. EDLC stores charge via the electrosorption of ions at the electrode/electrolyte interface. This mechanism typically restricts the capacitance of the electrode materials within 300 F g^{-1}, owing to the limited surface area of involved materials[4,5]. Contrary to EDLC, pseudocapacitors involving materials such as transition metal compounds[6,7] and conducting polymers[8] can achieve significantly higher capacitance owing to their reliance on surface Faradic redox reaction. However, pseudocapacitive materials often experience poor electrical conductivity and structural instability during continuous cycling, resulting in inferior rate capability and cycle performances. Thus, the advancement of supercapacitor technology relies heavily on developing high-performance pseudocapacitive materials that demonstrate higher rate capability and extended lifespan.

Among the emerging materials, MXenes, a class of two-dimensional (2D) transition metal carbides, nitrides, and carbonitrides, produced typically from ternary $M_{n+1}AX_n$ precursors via selectively etching the A atom layers (mainly IIIA and IVA group elements) are getting immense recognition as advanced energy storage materials. MXenes have a representative formula of $M_{n+1}X_nT_x$, where M is early transition metals, X is carbon and/or nitrogen with n between 1~4, and T is the associated terminations (-O, -OH, and -F)[9-12]. Their unique structural configuration, inherited from MAX phases, gives them metallic conductivity, rich surface chemistry, high density, hydrophilicity, and excellent flexibility, recognizing them as a promising electrode material[13,14]. Specifically, the 2D lamellar-like structure of MXene makes it versatile for the construction of flexible film electrodes, which are ideal for application in portable and wearable microelectronic devices[15,16]. For example, a MXene film prepared through blade-assisted coating can exhibit high conductivity (15,100 S cm^{-1} at 214 nm thickness), high tensile strength (~570 MPa at 940 nm thickness), and excellent flexibility, allowing the film to withstand numerous deformations[13]. Although such a configuration is promising, MXene flakes arranged face-to-face might cause significant layer-restacking due to high interlayer van der Waals forces, undermining the surface-active sites and extended ion diffusion pathways and thus causing low capacitance and inferior kinetics.

To address the problem of MXene-layer restacking, the structural modification of densely packed MXene films into open designs, for example, 3D configurations[17,18] and vertical arrays[19], has become a favorable approach. This can be achieved through various methods, including template methods[20,21], self-assembly[22], mechanical shearing[19], and 3D printing[23]. For example, poly(methyl methacrylate) spheres have been reported as a template to facilitate the fabrication of hollow MXene spheres, which, when accumulated, form macroporous MXene films with exposed active surfaces and developed ion diffusion channels[24]. However, the macroporous structure significantly decreases the film density (0.25~0.4 mg cm^{-3}), thus deteriorating the electrode's volumetric performance. Additionally, modulating the structure of the precursor has proven effective in enlarging the interlayer spacing of the MXene films[25]. A hexagon Ti_3AlC_2

with a spiral chiral symmetry structure may be pre-stratified using a Lewis acid molten salt technique and etched using a microwave-assisted procedure to form an MXene film with a large interlayer spacing of 1.39 nm and excellent structural stability. Among other strategies, the use of "interlayer spacers" such as graphene[26], carbon nanotubes (CNTs)[27], and celluloses[28] has also shown promising results in effective modulation of the interlayer structure of MXene films.

Our previous work demonstrated the improved ion transportability of CNT-intercalated MXene films, achieving a high capacitance (200 F g^{-1} at 500 A g^{-1}) compared to its pristine counterpart (153 F g^{-1}). Nevertheless, similar capacitances observed at lower rates suggest inadequate exposure to surface active sites, limiting capacitance improvement[29]. At the same time, the spacer-intercalated MXene films may also suffer from decreased film density due to the increased interlayer spacing. Therefore, developing a simple yet efficient strategy to fabricate flexible, open MXene architectures without compromising the integrity and film density remains a significant challenge.

Herein, we propose a rationally designed MXene film electrode from the perspective of inducing microscopical disorder. This MXene film was constructed via the integration of gelatin into MXene flakes followed by carbonization for the *in-situ* formation of CDs that act as intercalators, enabling increased interlayer spacing and disorder while preventing layer restacking and exposing MXene active sites, ensuring rapid ion diffusivity and superior electrode kinetics. Meanwhile, the carbonization removes ineffective surface groups, resulting in high-density carbon dots-intercalated MXene films (CDs-MF). The CDs-MF, when tested as an electrode, demonstrated improved capacitive performances compared to its pristine counterpart with a high gravimetric capacitance of 396.4 F g^{-1} at 1 A g^{-1} and a volumetric capacitance of 1,153.2 F cm^{-3} at 1 A cm^{-3}. Moreover, the assembled flexible symmetric supercapacitor (SSC) realized a volumetric energy density of 21.2 Wh L^{-1} while maintaining excellent capacitive performance under various operating conditions.

EXPERIMENTAL

Preparation of CDs-MF

The CDs-MF was prepared by intercalating gelatin molecules within the MXene interlayers, followed by a carbonization process. First, a 1 mg mL^{-1} flaxen and translucent solution was prepared by rapidly stirring gelatin powder in deionized water (DIW) at 45 °C. The solution was then added to the MXene dispersion under stirring (10 min) in varying mass ratios (3%, 5%, and 10 wt.%) to form a uniform blend. Subsequently, the gelatin/MXene blend was vacuum filtrated to achieve gelatin-intercalated MXene films (G-MF). The films were labeled as G-MF-1, G-MF-2, and G-MF-3, corresponding to gelatin mass ratios of 3%, 5%, and 10 wt.%, respectively. Finally, the G-MF films were subjected to an annealing process (400 °C, 2 h) under a flowing Ar atmosphere, resulting in CDs-MF films with differently intercalated CDs (CDs-MF-1, CDs-MF-2, and CDs-MF-3 films). For comparison, pristine MXene film (p-MF) was produced via a direct vacuum filtration of MXene dispersion, whereas annealed film (a-MF) was prepared similarly to CDs-MF but without gelatin.

RESULTS AND DISCUSSION

Figure 1A depicts the intercalation of the gelatin molecules within the MXene interlayers, followed by the carbonization-enabled fabrication of CDs-MF. Initially, accordion-like Ti_3AlC_2 [Supplementary Figure 1A] was etched by LiF/HCl to produce multilayer $Ti_3C_2T_x$, followed by ultrasonication to exfoliate multilayers into single or few-layer MXene flakes with excellent aqueous dispersity [Supplementary Figure 2 and 3]. The corresponding X-ray diffraction (XRD) pattern exhibits a characteristic (002) peak of $Ti_3C_2T_x$ at 7° [Supplementary Figure 3B], which was lower than that of the Ti_3AlC_2 (9.5°) [Supplementary Figure 1B],

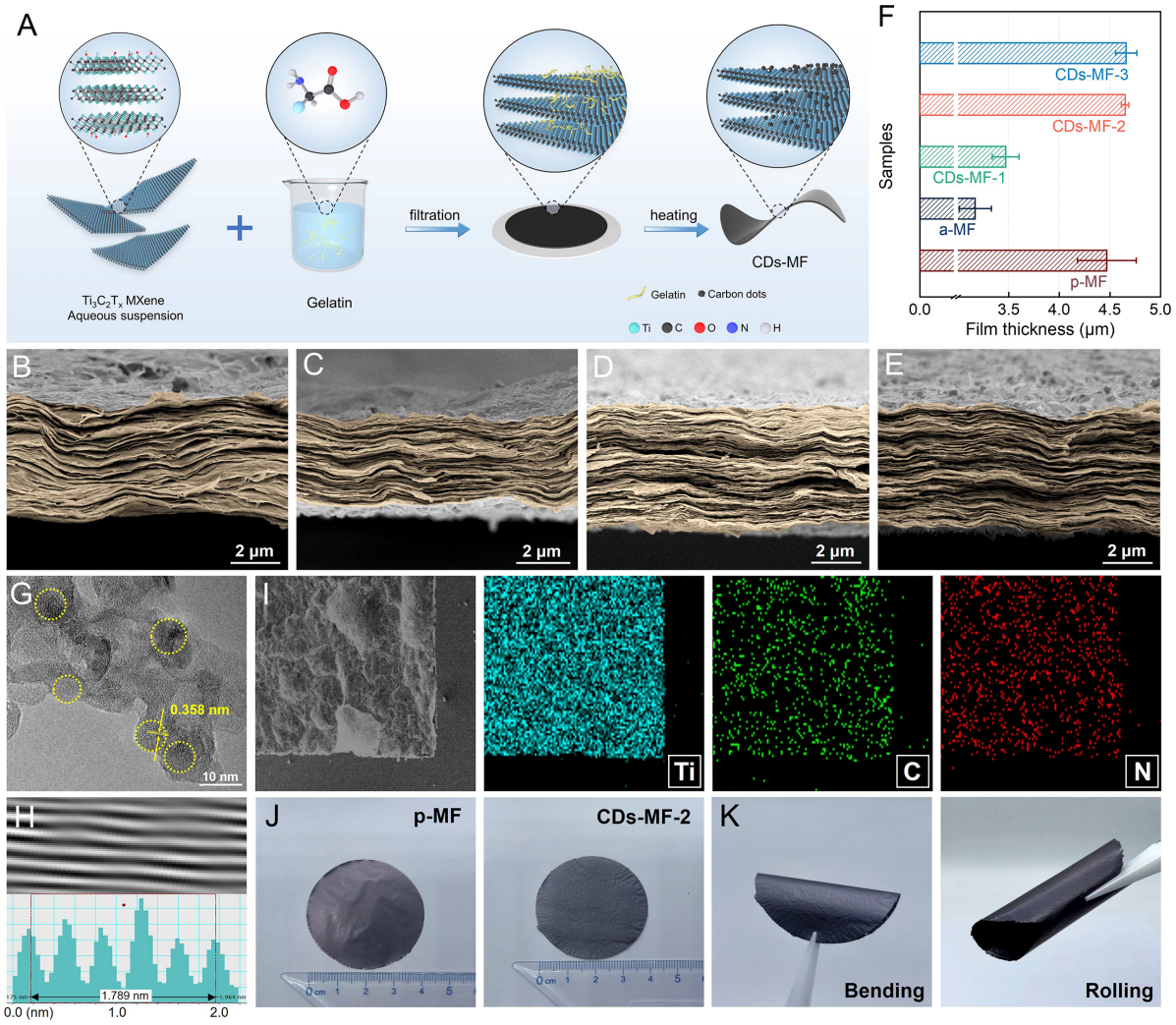

Figure 1. (A) Schematic diagram illustrating the fabrication process of CDs-MF, cross-sectional SEM images of the (B) p-MF, (C) CDs-MF-1, (D) CDs-MF-2, and (E) CDs-MF-3 and corresponding (F) film thickness variation, (G and H) HRTEM image of the specific regions of CDs-MF-2 with corresponding lattice fringe and FFT pattern, (I) SEM image (top-view) of the CDs-MF-2 and corresponding energy-dispersive X-ray spectroscopy (EDS) mapping showing Ti, C, and N elements, (J) comparison of surface macroscopic morphology of the CDs-MF-2 and p-MF, (K) flexibility of CDs-MF-2 film, withstanding bending and rolling without structural damage.

confirming the successful etching process. The MXene dispersion was mixed with gelatin solution and subjected to vacuum filtration, allowing the gelatin to intercalate within MXene flakes. The resulting G-MF exhibited a flake-stacked structure, slightly less ordered than p-MF [Supplementary Figure 4]. In G-MF-3, the MXene flakes were closely packed due to the high gelatin content. Finally, the G-MFs were annealed to *in-situ* carbonize the gelatin into CDs, forming CDs-MF architectures.

Cross-sectional scanning electron microscope (SEM) images of the CDs-MF in reference to their p-MF and a-MF counterparts are presented in Figure 1B-E and Supplementary Figure 5. Despite exhibiting similar microscopic morphologies, the film thickness varied significantly among CDs-MF, p-MF, and a-MF, as summarized in Figure 1F. The thicknesses of the p-MF and a-MF were measured at 4.47 ± 0.29 and 3.17 ± 0.16 μm, respectively. The decrease in the thickness of a-MF compared to p-MF is attributed to MXene surface terminations removal and increased layer restacking post-annealing. In contrast, *in-situ*

intercalated CDs substantially expanded the MXene film. As a result, the CDs-MF-1, CDs-MF-2, and CDs-MF-3 exhibited film thicknesses of 3.47 ± 0.13, 4.65 ± 0.04, and 4.66 ± 0.11 μm, respectively, signifying the enlarged interlayer spacings in CDs-MF that contribute to exposing active surface regions and facilitating ion diffusion in the electrode.

Figure 1G and H depict the high-resolution transmission electron microscope (HRTEM) image of the CDs-MF-2 and the fast Fourier transform (FFT) pattern, revealing numerous nano-size particles (< 10 nm) on the MXene flakes post-annealing. The lattice fringe of these nanoparticles was determined to be ~0.358 nm, corresponding to the (002) crystal plane of carbon, indicating the CDs-intercalated nature of the CDs-MF-2[29,30]. Given that the amino groups in the gelatin chain led to nitrogen doping during carbonization, the distribution of CDs within CDs-MF was confirmed through elemental mapping [Figure 1I]. Ti, C, and N element mappings corroborated the homogeneous CD intercalation throughout the MXene film. Figure 1J shows the surface macroscopic morphologies of the CDs-MF-2 and p-MF, where CDs-MF-2 appear tarnished and coarsened due to the *in-situ* intercalation of CDs during annealing. Despite these changes, CDs-MF-2 maintained excellent flexibility, as demonstrated by its ability to withstand various deformations such as bending and rolling [Figure 1K]. This confirms its potential as a flexible supercapacitor electrode for wearable electronic devices.

The electrical conductivities of CDs-MF, p-MF, and a-MF were investigated and are presented in Figure 2A. The p-MF exhibited an electrical conductivity of 2,764 ± 57 S cm^{-1}, which significantly decreased after the intercalation of insulating gelatin due to reduced electrical contact between the MXene flakes [Supplementary Figure 6]. The conductivity of a-MF reached 4,687 ± 303 S cm^{-1} after annealing due to the partial elimination of MXene surface terminations and improved flake orientation[13]. Upon intercalation of CDs within the MXene, the electrical conductivity of CDs-MF decreases with increasing CD content due to the successively enlarged interlayer spacing and microscopic disorder. Specifically, the conductivities of the CDs-MF-1, CDs-MF-2, and CDs-MF-3 were measured to be 4,554 ± 344, 3,493 ± 454, and 2,195 ± 321 S cm^{-1}, respectively. Despite this reduction, the electrical conductivities of CDs-MF remained competitive compared to p-MF, ensuring excellent electron transportation within the electrode. The film densities of the electrodes are summarized in Figure 2B. The p-MF exhibited a film density of 2.74 ± 0.12 g cm^{-3}, which increased to 3.86 ± 0.17 g cm^{-3} for the a-MF due to the significantly decreased film thickness. In contrast, the intercalated CDs expanded the film thickness of a-MF, resulting in reduced film densities for the CDs-MF. Specifically, CDs-MF-1 achieved a film density of 3.52 ± 0.15 g cm^{-3}, which decreased to 2.85 ± 0.13 and 2.73 ± 0.11 g cm^{-3} with increasing CD content within MXene film. Nevertheless, the CDs-MF films demonstrate superior film density compared to the p-MF, which is beneficial for achieving excellent volumetric performance for supercapacitive applications.

XRD analysis was employed to investigate the variation of interlayer spacings of the CDs-MF, p-MF, and a-MF [Figure 2C and D]. The variations in interlayer spacings of these MXene-based electrodes positively correlate with their respective thickness changes. Specifically, the a-MF exhibited a right-shifted (002) peak at 7.5° compared to p-MF, indicating reduced interlayer spacing from 12.6 to 11.8 Å, subsequent to the partial surface terminations elimination and the deteriorated layer-restacked structure. In contrast, the intercalation of gelatin molecules resulted in lower-angle (002) peaks for G-MF compared to p-MF [Supplementary Figure 7]. The (002) peak of CDs-MF-1, following CD intercalation, exhibited a similar feature to that of the a-MF, implying no significant interlayer structure change occurred due to the inadequate CD intercalation. However, a notable shift was observed in the CDs-MF-2 with increased CD content. The (002) peak of CDs-MF-2 was positioned at 6.6°, indicating a 13.4 Å interlayer spacing. As the CD content continued to increase, the CDs-MF-3 displayed a marginally downward shift in the (002) peak

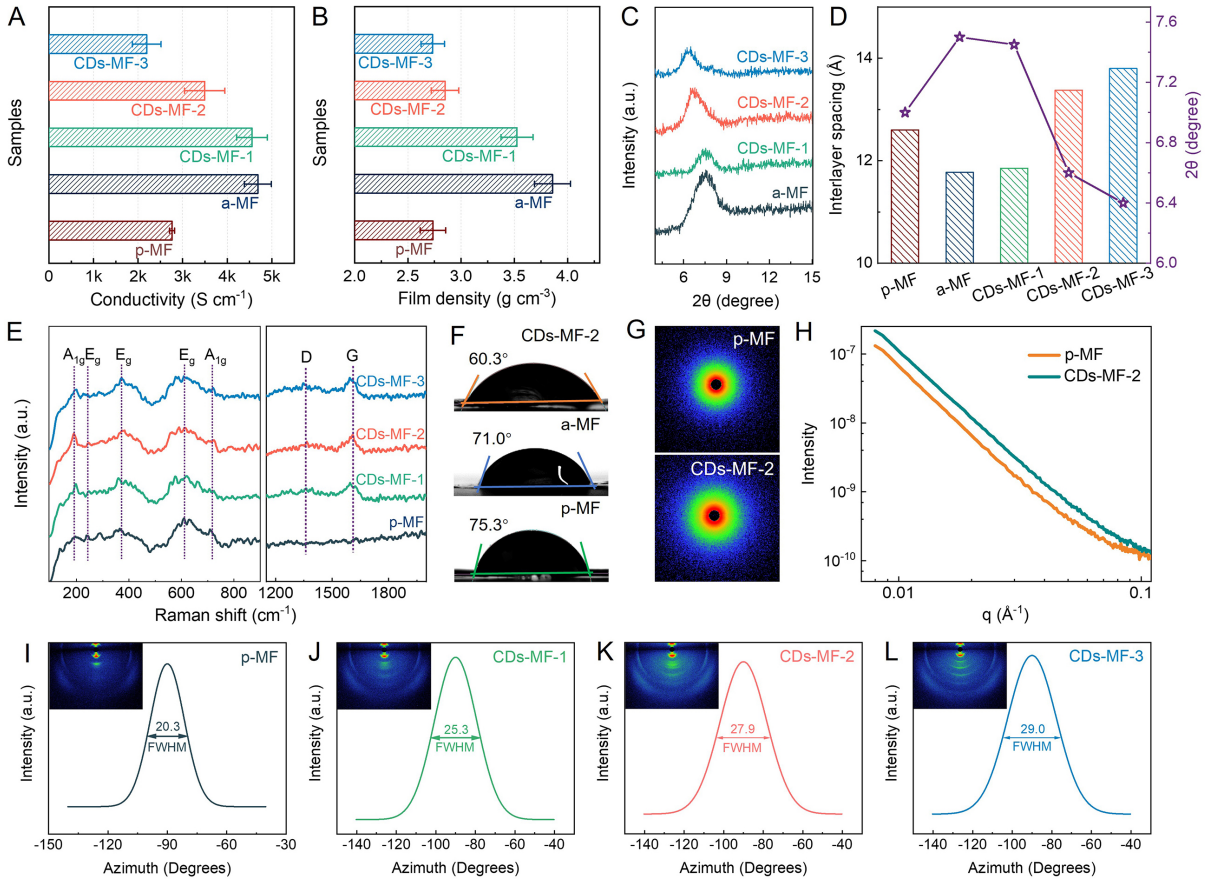

Figure 2. (A) Electrical conductivities, (B) film densities, (C) XRD patterns of CDs-MF and their corresponding (D) interlayer spacing variation, (E) Raman spectra of the CDs-MF, (F) water contact angles of the CDs-MF-2, a-MF, and p-MF, (G and H) SAXS scattering intensities of the CDs-MF-2 and p-MF, WAXS patterns of the (I) p-MF, (J) CDs-MF-1, (K) CDs-MF-2, and (L) CDs-MF-3 showing their FWHM.

location to 6.4°, aligning with the observations made regarding film thickness. Figure 2E presents the Raman spectra of CDs-MF compared to p-MF counterpart, showing similar peak profiles in the range of 100~1,000 cm^{-1}, including the A_{1g} symmetric out-of-plane vibrational peaks near 188 and 720 cm^{-1}, and E_g shear vibrational peaks at 246, 369, and 611 cm^{-1}[20,31]. The absence of TiO_2 vibrational states confirms the well-preserved structure of MXene with no oxidation post-*in situ* CD intercalation. Notably, distinct D and G carbon bonds were observed for the CDs-MF near 1363 and 1607 cm^{-1}, confirming their successful intercalation with CDs[32,33].

Water contact angle measurement confirmed the variation in wettability for the CDs-MF, a-MF, and p-MF. In Figure 2F, p-MF had a water contact angle of 75.3°, which decreased to 71° and 60.3° for a-MF and CDs-MF-2, respectively, confirming improved hydrophilicity with the rise of CD intercalation. This increased hydrophilicity is beneficial for permeating aqueous electrolytes and ion diffusion within the electrode. X-ray photoelectron spectroscopy (XPS) confirmed the surface chemical variation of CDs-MF-2 compared to the p-MXene counterpart. The C 1s binding energy profile for CDs-MF-2 was deconvoluted into major binding energies for C-Ti, C-Ti-O, C-C, C-O, and O-C=O bonds at 281.6, 282.9, 284.6, 285.8, and 288.6 eV, respectively [Supplementary Figure 8][20,34]. As seen, the intercalation of CDs has strengthened the C-C bond in CDs-MF-2 compared to p-MXene. Supplementary Figure 9 shows the O 1s binding energy profiles of the CDs-MF-2 and p-MF, with the latter exhibiting four peaks associated with Ti-O, C-Ti-O_x, C-Ti-$(OH)_x$, and

H_2O_{ads} at 530.1, 531.1, 532.2, and 533.8 eV, respectively[35-37]. In contrast, the CDs-MF-2 exhibited a similar profile with an additional peak of C=O at 531.7 eV, owing to intercalated CDs and the annealing treatment[38-40].

Given the significant differences in the interlayer structures, film density, electrical conductivity, and surface chemistry between CDs-MF and p-MF owing to *in-situ* CD intercalation, small-angle X-ray scattering (SAXS) and wide-angle X-ray scattering (WAXS) measurements were conducted to elucidate the porosity and orientation degree of the MXene flakes. The SAXS pattern of CDs-MF-2 exhibited lower intensity than p-MF, confirming developed porosity [Figure 2G and H][41]. The (002) peak azimuth diagram and full width at half maximum (FWHM) were analyzed through WAXS patterns [Figure 2I-L]. The p-MF showed a FWHM value of 20.3°, which increased to 25.3, 27.9, and 29.0° for the CDs-MF-1, CDs-MF-2, and CDs-MF-3, respectively. Correspondingly, the orientation degree factor (Π), which signifies the flake orientation degree relative to the film plane, was calculated [Π = (180° - FWHM)/180° × 100%][42]. The high Π value of 88.7% indicates an ordered p-MF structure aligned with the horizontal axis of the 2D assembly. In contrast, the CDs-MF showed decreased Π values of 85.9%, 84.5%, and 83.9% with increasing CD intercalation, demonstrating progressively developed microscopic disorder[43,44]. The highly ordered orientation of MXene flakes in p-MF imparts characteristics such as high electrical conductivity and low interlayer spacing, whereas the developed porosity in CDs-MF allows for exposed active surfaces and convenient ion transport channels, resulting in improved capacitive performance.

The capacitive characteristics of CDs-MF were assessed in a three-electrode setup with activated carbon as a counter electrode and a 3 M H_2SO_4 electrolyte. Figure 3A compares the cyclic voltammetry (CV) curves of CDs-MF, p-MF and a-MF at a scan rate of 5 mV s^{-1} in the potential range of -0.6~0.2 V (*vs.* Ag/AgCl). All samples exhibited similar peak profiles with distinct redox peaks, confirming their pseudocapacitive nature. The redox chemistry stems from MXene's reversible proton intercalation/de-intercalation and Ti atom oxidation variation[24,45]. The increased integral CV areas of CDs-MF, compared to p-MF, suggest greater capacitances resulting from the expanded interlayer spacing and exposed surface-active sites of CDs intercalated MXene after annealing. The a-MF, characterized by its reduced interlayer spacing, had a CV curve encompassing its p-MF counterpart due to the exposed redox active sites on the MXene surface after annealing[46]. Figure 3B shows the galvanostatic charge-discharge (GCD) curves of the CDs-MF, a-MF, and p-MF at 1 A g^{-1}, where all samples realized approximately symmetric nonlinear profiles differing from the typical triangle-like profile of EDLC, further corroborating the electrode's inherent pseudocapacitive mechanism. Among all, the CDs-MF-2 had the longest duration for the charge-discharge cycle, indicating its superior capacitance performance.

Figure 3C and Supplementary Figure 10 show the CV profiles of the electrodes at different scan rates. The p-MF and a-MF show distorted profiles in comparison to CDs-MF, which retains its peak patterns even at scan rates exceeding 200 mV s^{-1}, confirming the superiority of intercalated CDs in promoting ion diffusion and accessibility, thereby improving its overall electrochemical performance at high current rates. Correspondingly, the gravimetric capacitances of CDs-MF calculated from the CV curves at different scan rates are provided in Supplementary Figure 11 and Supplementary Table 1. As seen, CDs-MF offers significantly improved capacitance compared with the a-MF and p-MF, highlighting the advantages of CD intercalation within MXenes film.

The gravimetric capacitances of CDs-MF, a-MF, and p-MF at current densities ranging from 1 to 1,000 A g^{-1} are shown in Figure 3D. As seen, the p-MF realized a capacitance of 258.8 F g^{-1} at 1 A g^{-1}, which then increased to 325.7 F g^{-1} post-annealing due to exposure of additional active surface sites. In contrast, the

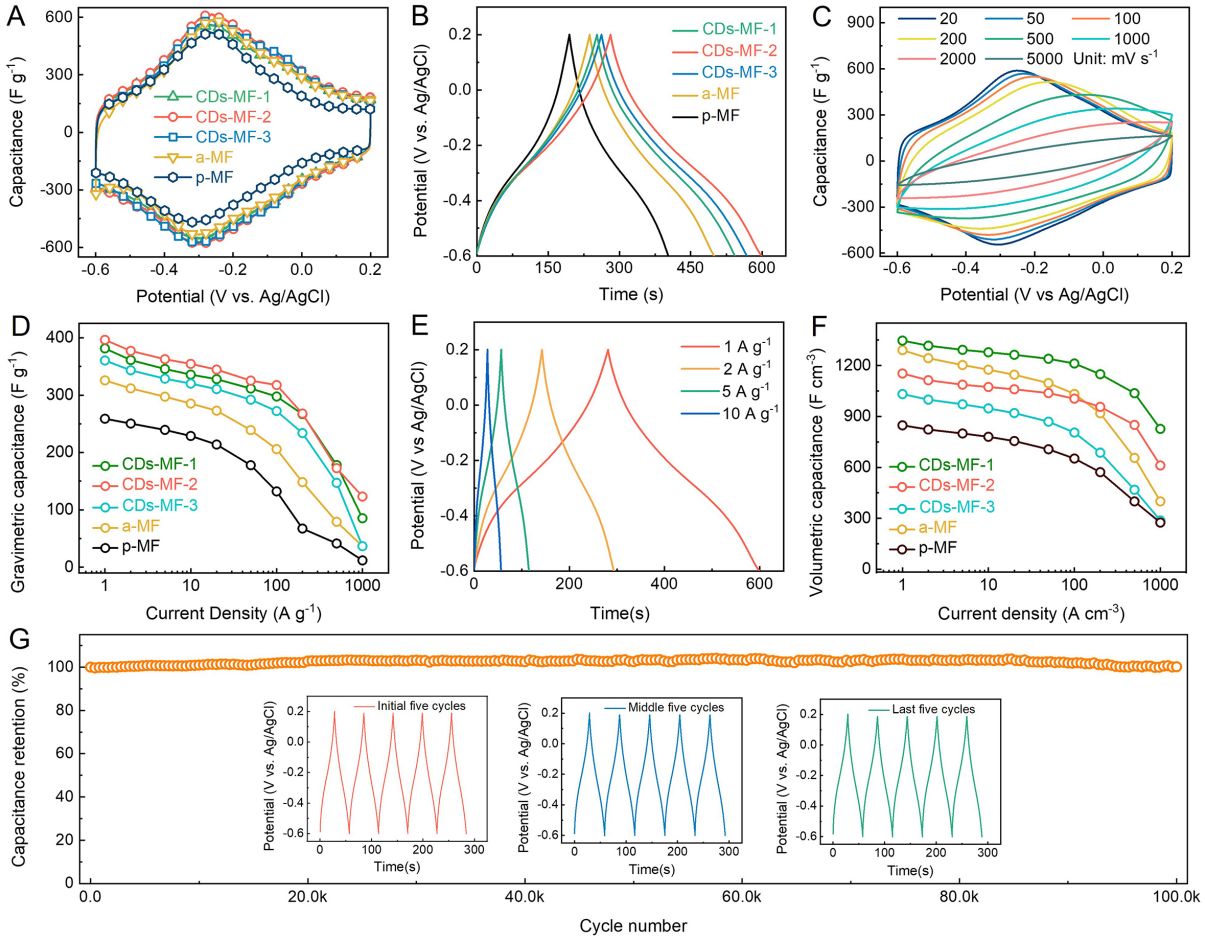

Figure 3. Electrochemical performances of the CDs-MF in reference to p-MF and a-MF counterparts, (A) CV curves at 5 mV s^{-1}, (B) GCD curves at 1 A g^{-1}, (D) gravimetric capacitances, and (F) volumetric capacitances of the CDs-MF, p-MF, and a-MF at various current densities, (C) CV curves at different scan rates and (E) GCD curves at different current densities of the CDs-MF-2, (G) long-term cycle performance of the CDs-MF-2 at 10 A g^{-1} with inset depicting its initial, middle, and last 5 GCD curves.

intercalation of CDs endowed the CDs-MF with enlarged interlayer spacings and developed microscopic disorder, resulting in high capacitances of 381.5, 396.4, and 360.3 F g^{-1} for the CDs-MF-1, CDs-MF-2, and CDs-MF-3, respectively. Remarkably, even at 1,000 A g^{-1}, the CDs-MF-2 maintained a high capacitance of 123.2 F g^{-1}, outperforming the p-MF (11.9 F g^{-1}) and a-MF (36.6 F g^{-1}) counterparts. This improved capacitive behavior validates the superiority of CD intercalation in enhancing ion transportation and accessibility within MXene film, thus achieving excellent rate capability. In addition, even at current densities as high as 200 A g^{-1}, the GCD curves of CDs-MF-2 showed symmetrical nonlinear profiles [Figure 3E and Supplementary Figure 12], confirming the electrode's excellent reversibility. Additionally, the capacitances of CDs-MF-2 were compared to previously reported MXene-based electrodes at varying current densities [Supplementary Figure 13]. The CDs-MF-2 exhibits competitively superior performances in capacitance and rate capability, highlighting its potential as a high-performance supercapacitive material.

The high density and excellent gravimetric performance also contribute to outstanding volumetric performance of CDs-MF. As shown in Figure 3F, the p-MF achieved a volumetric capacitance of 847.6 F cm^{-3} at 1 A cm^{-3}, which rapidly declined to 274.8 F cm^{-3} when the current density reached 1,000 A cm^{-3}. In contrast, the exposed active surface and improved ion transportability enabled the CDs-MF

to have much enhanced volumetric capacitances and rate capability. Specifically, CDs-MF-2 exhibited a volumetric capacitance of 1,153.2 F cm^{-3} at 1 A cm^{-3}, with a capacitance retention of 53.3% at 1,000 A cm^{-3}, much higher than p-MF (32.4%). Due to the high density of 3.5 g cm^{-3}, CDs-MF-1 outperformed CDs-MF-2 in volumetric capacitance, obtaining 1,347.0 and 826.8 F cm^{-3} at 1 and 1,000 A cm^{-3}, respectively. The exceptional gravimetric and volumetric performances of CDs-MF-2 showcase its potential application in wearable and portable electronics. Furthermore, the extended cycling of the CDs-MF-2 was tested at 5 and 10 A g^{-1}, as depicted in Figure 3G and Supplementary Figure 14. The CDs-MF-2 achieved excellent cycling stability at 5 A g^{-1}, exhibiting no capacitance decay over 8,000 cycles. More importantly, it can withstand an ultralong charge/discharge cycling up to 100,000 times at 10 A g^{-1}. The GCD curves of CDs-MF-2 remained consistent throughout the first, middle, and final five cycles, signifying its extraordinary cycling stability and reversibility.

Electrochemical impedance spectroscopy (EIS) analysis was conducted to investigate the electrode kinetics of the CDs-MF-2 and p-MF. The Nyquist plots show that the straight line of CDs-MF-2 in the low-frequency region is almost perpendicular to the longitudinal axis and larger than that of the p-MF [Figure 4A]. The relationship between Z' and ω ($\omega = 2\pi f$) in the low-frequency region demonstrated a much lower slope for the CDs-MF-2 compared to p-MF [Supplementary Figure 15]. These results confirm the significantly improved ion diffusion capability within CDs-MF-2 due to the *in-situ* intercalation of CDs. Moreover, the evolution of impedance characteristics for CDs-MF-2 was assessed through daily EIS curves during a 21-day immersion in 3 M H_2SO_4 electrolyte. As shown in Supplementary Figure 16, the CDs-MF-2 exhibited a pronounced decrease in charge transfer impedances over time, attributable to the gradual infiltration of electrolyte ions into the MXene interlayer, thereby activating the electrode. In contrast, the equivalent series resistance (the x-intercept in the high-frequency region) remains constant across the entire 21-day immersion period, signifying the remarkable structural stability of the CDs-MF-2 in H_2SO_4 electrolyte. The impedance behaviors of the CDs-MF-2 and p-MF were further analyzed using the complex model of capacitance C(ω), which includes a real part of C′(ω) and an imaginary part C″(ω) [Figure 4B and C][47,48]. CDs-MF-2 exhibited a higher normalized C′(ω) that decreases much slower than the p-MF with increasing frequency. The relaxation time constant (τ_0, minimal time needed to discharge energy with above 50% efficiency) was determined to be 2.49 s for CDs-MF-2, significantly lower than p-MF (4.87 s), corroborating the former faster ion diffusion ability.

The charge storage kinetics of the CDs-MF-2 and p-MF were evaluated from the power law equation describing the peak current (i) and scan rate (v) relationship [Supplementary Equation 3][49-51]. The b values of p-MF in the cathodic/anodic scan were 0.88 and 0.89, respectively [Figure 4D and E]. In contrast, the b values of CDs-MF-2 increased to 0.95 and 0.93, reflecting the predominance of capacitive-controlled contribution to the total capacitance. The specific contributions at different scan rates calculated via representative Supplementary Equation 4 are shown in Figure 4F. As seen, CDs-MF-2 achieved a capacitive-controlled contribution of 84% at 5 mV s^{-1}, which increased to 97% as the scan rate approached 200 mV s^{-1}. For comparison, only 64% of the capacitance originated from the capacitive-controlled behavior at 5 mV s^{-1} for the p-MF due to its densely stacked structure. The predominated capacitive behavior of CDs-MF-2 ensures fast charge transfer on the MXene surface even at high rates, resulting in high capacitance and superior rate capability.

A flexible SSC was configured to assess the practicality of the CDs-MF-2. Figure 5A shows two identical CDs-MF-2 electrodes configured within polyethylene terephthalate (PET) packages with a 3 M polyacrylic acid (PAA)/H_2SO_4 gel electrolyte. Figure 5B shows the CV curves of the CDs-MF-2 SSC at various scan rates (5 to 200 mVs^{-1}), depicting non-significant distortion with the increasing scan rates, further corroborating

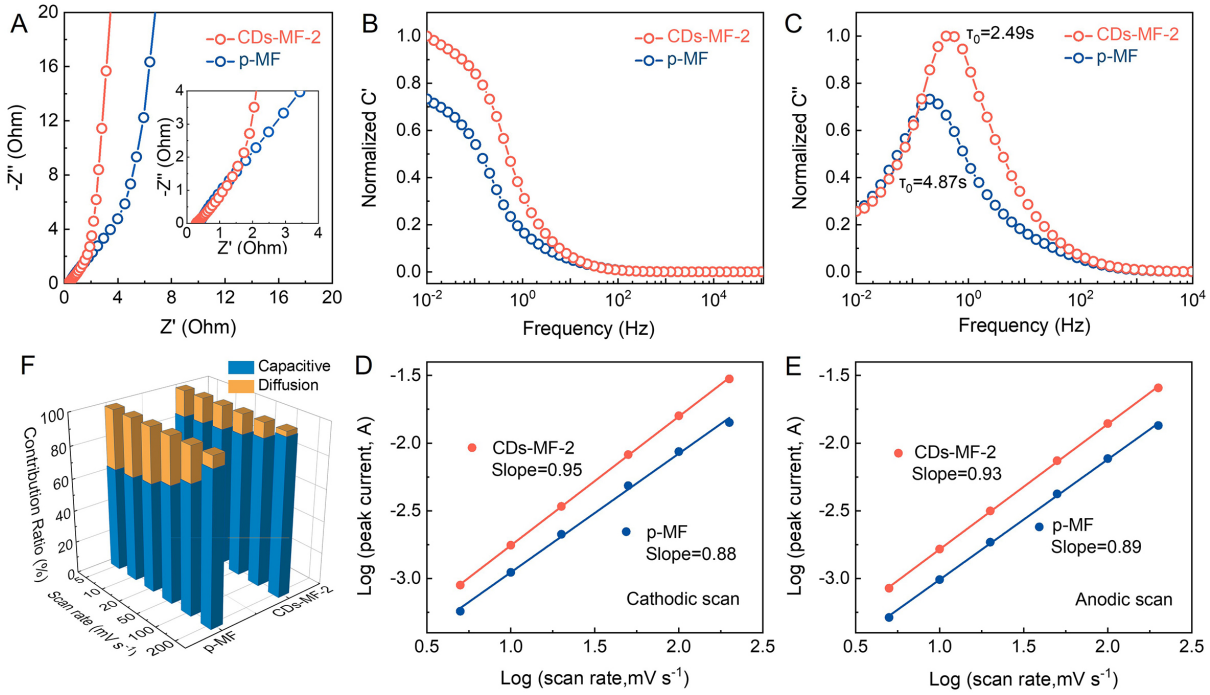

Figure 4. (A) Nyquist plots, (B) normalized real and (C) imaginary capacitances as a function of the frequency of the CDs-MF-2 and p-MF, (D and E) relationship between the peak current and scan rates, (F) capacitive distribution for the CDs-MF-2 and p-MF at different scan rates.

its superior high-rate endurance and reversibility. The extended cycling of the CDs-MF-2 SSC was evaluated at 10 A g^{-1} [Figure 5C]. The electrode maintained 94% of its original capacitance after 10,000 consecutive cycles, demonstrating its exceptional cycling stability. Furthermore, the Ragone plot of CDs-MF-2 SSC [Figure 5D] indicated a maximum energy density of 21.2 Wh L^{-1} at a power density of 112 W L^{-1} (based on the total mass of CDs-MF-2 electrode). Even when the power density was raised to 12 kW L^{-1}, the constructed SSC maintained an energy density of 12.3 Wh L^{-1}, highlighting the competitive superiority of CDs-MF-2 for supercapacitive applications.

Figure 5E and F shows that the CV curves of the SSC at different bending angles of 0°, 45°, 90°, and 180° were almost identical, indicating excellent mechanical robustness of the device, capable of withstanding large deformation without compromising the electrochemical performance. The practical application potential of SSC was further assessed by operating two devices in series or parallel to fulfill high voltage and capacitance demands. The corresponding CV and GCD curves [Figure 5G and H] show that series-assembled SSC had a working voltage of 1.6 V, double that of a single SSC. In contrast, the parallel-assembled device achieved doubled current output and discharge time, confirming the promising application of CDs-MF-2 in flexible and wearable devices.

CONCLUSIONS

A flexible, highly conductive, and microscopically disordered MXene film electrode was successfully designed using a simple *in-situ* CD intercalation process. Gelatin, pre-intercalated within MXene, transformed into CDs during annealing, which acted as interlayer spacers to expand the interlayer spacing and induce microscopic disorder between the MXene flakes, resulting in exposed active sites and rapid ion diffusivity, thereby achieving excellent kinetics. Consequently, the optimal CDs-MF-2 electrode delivered a

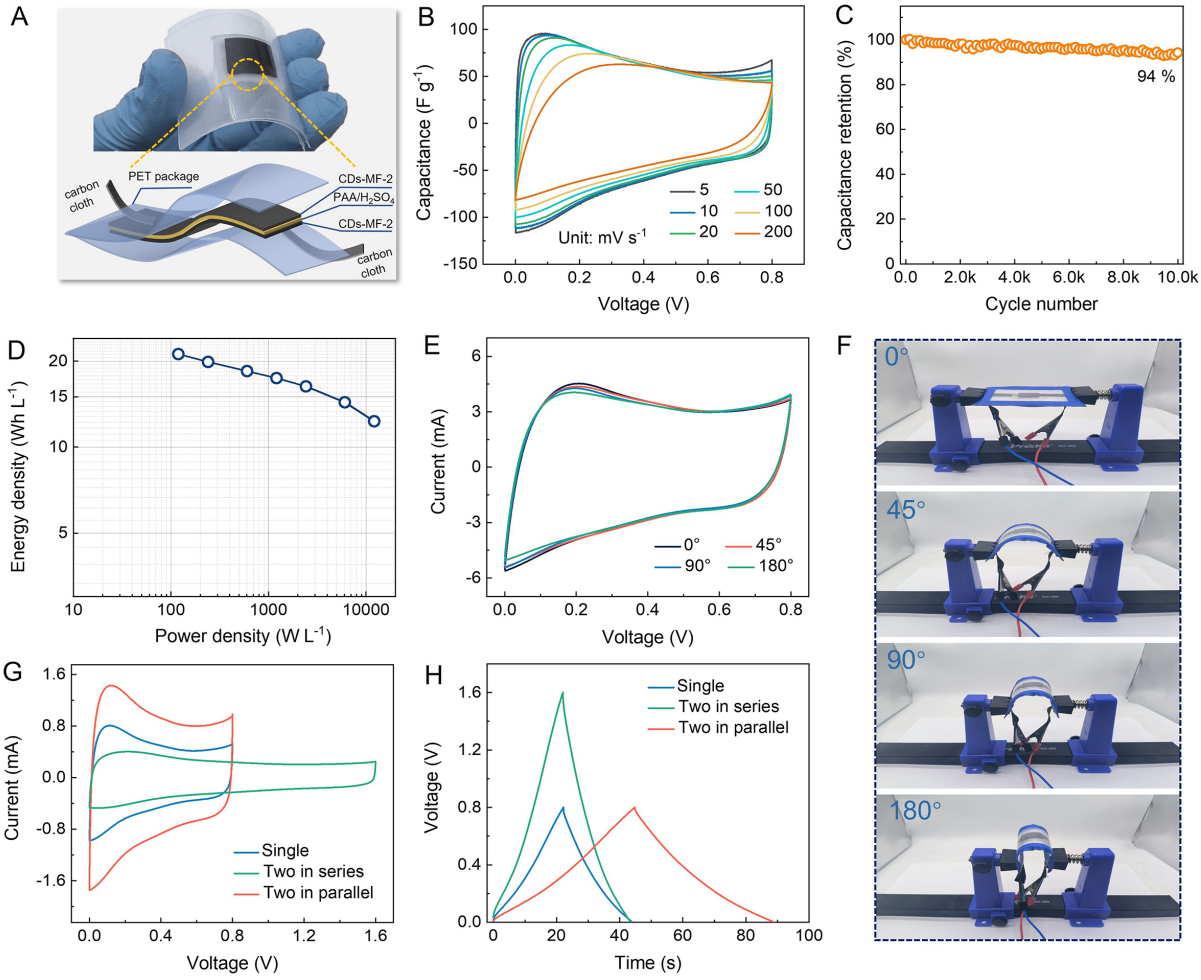

Figure 5. (A) Digital photograph and a structure illustration of the assembled CDs-MF-2 SSC, and corresponding (B) CV curves at various scan rates, (C) cycle performance at 10 A g^{-1} and (D) Ragone plots of the CDs-MF-2 SSC, (E) CV curves and (F) digital photographs of the CDs-MF-2 SSC at 0°, 45°, 90°, and 180° degree bends, (G) CV curves at 20 mV s^{-1} and (H) GCD curves at 2 A g^{-1} of two SSC connected in series and parallel.

high gravimetric capacitance of 396.4 F g^{-1} at 1 A g^{-1}, a superior rate capability of 123.2 F g^{-1} at 1,000 A g^{-1}, and an impressive cycle stability with no capacitance decay over 100,000 cycles. Moreover, the high-density characteristics of CDs-MF-2 and CDs-MF-3 resulted in high volumetric capacitances of 1,153.2 and 1,347.0 F cm^{-3}. When assembled in an SSC device, CDs-MF-2 realized a maximum energy density of 21.2 Wh L^{-1} and a power density of 12 kW L^{-1}. The SSC maintained its capacitive performance under various operating conditions, including bending at multiple angles and configurations in series or parallel assemblies. These results demonstrate the superiority of CD intercalation in MXene film electrodes for developing high-performance supercapacitors, making them suitable for use in flexible and wearable electronics.

DECLARATIONS

Authors' contributions

Investigation, writing-original draft, data curation, visualization, formal analysis: Yang, D.

Investigation, validation, formal analysis: Cui, H.
Conceptualization, data curation, supervision, visualization, writing-review & editing, funding acquisition, project administration: Xu, B.; Zhang, P.
Writing-review & editing: Soomro, R. A.

Availability of data and materials
The data are made available upon request to authors.

Financial support and sponsorship
This work was financially supported by the National Natural Science Foundation of China (Grant No. U2004212), Postdoctoral Fellowship Program of CPSF (GZB20230191), China Postdoctoral Science Foundation (2023M740991), and Natural Science Foundation of Henan province (242300420312).

Conflicts of interest
All authors declared that there are no conflicts of interest.

Ethical approval and consent to participate
Not applicable.

Consent for publication
Not applicable.

REFERENCES
1. Simon, P.; Gogotsi, Y. Perspectives for electrochemical capacitors and related devices. *Nat. Mater.* **2020**, *19*, 1151-63. DOI PubMed
2. Wang, Y.; Song, Y.; Xia, Y. Electrochemical capacitors: mechanism, materials, systems, characterization and applications. *Chem. Soc. Rev.* **2016**, *45*, 5925-50. DOI
3. Simon, P.; Gogotsi, Y.; Dunn, B. Where do batteries end and supercapacitors begin? Electrochemical measurements can distinguish between different types of energy storage materials and their underlying mechanisms. *Science* **2014**, *343*, 1210-1. DOI PubMed
4. Yin, J.; Zhang, W.; Alhebshi, N. A.; Salah, N.; Alshareef, H. N. Synthesis strategies of porous carbon for supercapacitor applications. *Small. Method.* **2020**, *4*, 1900853. DOI
5. Li, T.; Ma, R.; Lin, J.; et al. The synthesis and performance analysis of various biomass-based carbon materials for electric double-layer capacitors: a review. *Int. J. Energy. Res.* **2020**, *44*, 2426-54. DOI
6. Xiao, X.; Song, H.; Lin, S.; et al. Scalable salt-templated synthesis of two-dimensional transition metal oxides. *Nat. Commun.* **2016**, *7*, 11296. DOI PubMed PMC
7. Wang, T.; Chen, H. C.; Yu, F.; Zhao, X. S.; Wang, H. Boosting the cycling stability of transition metal compounds-based supercapacitors. *Energy. Storage. Mater.* **2019**, *16*, 545-73. DOI
8. Naskar, P.; Maiti, A.; Chakraborty, P.; Kundu, D.; Biswas, B.; Banerjee, A. Chemical supercapacitors: a review focusing on metallic compounds and conducting polymers. *J. Mater. Chem. A.* **2021**, *9*, 1970-2017. DOI
9. Vahidmohammadi, A.; Rosen, J.; Gogotsi, Y. The world of two-dimensional carbides and nitrides (MXenes). *Science* **2021**, *372*, eabf1581. DOI PubMed
10. Zhou, S.; Zhang, P.; Li, Y.; et al. Ultrastable organic anode enabled by electrochemically active MXene binder toward advanced potassium ion storage. *ACS. Nano.* **2024**, *18*, 16027-40. DOI
11. Naguib, M.; Barsoum, M. W.; Gogotsi, Y. Ten years of progress in the synthesis and development of MXenes. *Adv. Mater.* **2021**, *33*, 2103393. DOI PubMed
12. Soomro, R. A.; Zhang, P.; Fan, B.; Wei, Y.; Xu, B. Progression in the oxidation stability of MXenes. *Nano-Micro. Lett.* **2023**, *15*, 108. DOI PubMed PMC
13. Zhang, J.; Kong, N.; Uzun, S.; et al. Scalable manufacturing of free-standing, strong $Ti_3C_2T_x$ MXene films with outstanding conductivity. *Adv. Mater.* **2020**, *32*, 2001093. DOI
14. Zhu, Q.; Li, J.; Simon, P.; Xu, B. Two-dimensional MXenes for electrochemical capacitor applications: progress, challenges and perspectives. *Energy. Storage. Mater.* **2021**, *35*, 630-60. DOI

15. Xu, X.; Guo, T.; Lanza, M.; Alshareef, H. N. Status and prospects of MXene-based nanoelectronic devices. *Matter* **2023**, *6*, 800-37. DOI
16. Zhu, Y.; Wang, S.; Ma, J.; Das, P.; Zheng, S.; Wu, Z. S. Recent status and future perspectives of 2D MXene for micro-supercapacitors and micro-batteries. *Energy. Storage. Mater.* **2022**, *51*, 500-26. DOI
17. Zhao, M. Q.; Xie, X.; Ren, C. E.; et al. Hollow MXene spheres and 3D macroporous MXene frameworks for Na-ion storage. *Adv. Mater.* **2017**, *29*, 1702410. DOI
18. Li, K.; Liang, M.; Wang, H.; et al. 3D MXene architectures for efficient energy storage and conversion. *Adv. Funct. Mater.* **2020**, *30*, 2000842. DOI
19. Xia, Y.; Mathis, T. S.; Zhao, M. Q.; et al. Thickness-independent capacitance of vertically aligned liquid-crystalline MXenes. *Nature* **2018**, *557*, 409-12. DOI
20. Zhang, P.; Zhu, Q.; Soomro, R. A.; et al. In situ ice template approach to fabricate 3D flexible MXene film-based electrode for high performance supercapacitors. *Adv. Funct. Mater.* **2020**, *30*, 2000922. DOI
21. Lv, K.; Zhang, J.; Zhao, X.; Kong, N.; Tao, J.; Zhou, J. Understanding the effect of pore size on electrochemical capacitive performance of MXene foams. *Small* **2022**, *18*, 2202203. DOI PubMed
22. Shang, T.; Lin, Z.; Qi, C.; et al. 3D macroscopic architectures from self-assembled MXene hydrogels. *Adv. Funct. Mater.* **2019**, *29*, 1903960. DOI
23. Yang, C.; Wu, X.; Xia, H.; et al. 3D printed template-assisted assembly of additive-free $Ti_3C_2T_x$ MXene microlattices with customized structures toward high areal capacitance. *ACS. Nano.* **2022**, *16*, 2699-710. DOI
24. Lukatskaya, M. R.; Kota, S.; Lin, Z.; et al. Ultra-high-rate pseudocapacitive energy storage in Two-dimensional transition metal carbides. *Nat. Energy.* **2017**, *2*, 17105. DOI
25. Wu, Q.; Xue, Y.; Li, P.; Wang, Y.; Wu, F. High specific capacitance and long cycle stability of few-layered hexagonal Ti_3C_2 free-standing film constructed with spiral chiral Hexagon Ti_3AlC_2. *Appl. Surf. Sci.* **2023**, *609*, 155329. DOI
26. Zhou, Y.; Maleski, K.; Anasori, B.; et al. $Ti_3C_2T_x$ MXene-reduced graphene oxide composite electrodes for stretchable supercapacitors. *ACS. Nano.* **2020**, *14*, 3576-86. DOI
27. Chen, H.; Yu, L.; Lin, Z.; et al. Carbon nanotubes enhance flexible MXene films for high-rate supercapacitors. *J. Mater. Sci.* **2020**, *55*, 1148-56. DOI
28. Chen, W.; Zhang, D.; Yang, K.; Luo, M.; Yang, P.; Zhou, X. MXene ($Ti_3C_2T_x$)/cellulose nanofiber/porous carbon film as free-standing electrode for ultrathin and flexible supercapacitors. *Chem. Eng. J.* **2021**, *413*, 127524. DOI
29. Zhao, Y.; Xue, K.; Yu, D. Y. W. Tuning Electrolyte solvation structure and CEI film to enable long lasting FSI^--based dual-ion battery. *Adv. Funct. Mater.* **2023**, *33*, 2300305. DOI
30. Tai, Z.; Zhang, Q.; Liu, Y.; Liu, H.; Dou, S. Activated carbon from the graphite with increased rate capability for the potassium ion battery. *Carbon* **2017**, *123*, 54-61. DOI
31. Sarycheva, A.; Gogotsi, Y. Raman spectroscopy analysis of the structure and surface chemistry of $Ti_3C_2T_x$ MXene. *Chem. Mater.* **2020**, *32*, 3480-8. DOI
32. Wei, Y.; Hou, W.; Zhang, P.; Soomro, R. A.; Xu, B. Bi_2S_3 nanorods encapsulated in iodine-doped graphene frameworks with enhanced potassium storage properties. *Chin. Chem. Lett.* **2022**, *33*, 3212-6. DOI
33. Zhang, P.; Li, J.; Yang, D.; Soomro, R. A.; Xu, B. Flexible carbon dots-intercalated MXene film electrode with outstanding volumetric performance for supercapacitors. *Adv. Funct. Mater.* **2023**, *33*, 2209918. DOI
34. Wang, M.; Cheng, Y.; Zhang, H.; et al. Nature-inspired interconnected Macro/Meso/Micro-porous MXene electrode. *Adv. Funct. Mater.* **2023**, *33*, 2211199. DOI
35. Halim, J.; Cook, K. M.; Naguib, M.; et al. X-ray photoelectron spectroscopy of select multi-layered transition metal carbides (MXenes). *Appl. Surf. Sci.* **2016**, *362*, 406-17. DOI
36. Bashir, T.; Ismail, S. A.; Wang, J.; Zhu, W.; Zhao, J.; Gao, L. MXene terminating groups =O, -F or -OH, -F or =O, -OH, -F, or =O, -OH, -Cl? *J. Energy. Chem.* **2023**, *76*, 90-104. DOI
37. Liu, Y.; Zhang, X.; Zhang, W.; et al. MXene-based quantum dots optimize hydrogen production via spontaneous evolution of Cl- to O-terminated surface groups. *Energy. Environ. Mater.* **2023**, *6*, 12438. DOI
38. Boidi, G.; Zambrano, D.; Broens, M. I.; et al. Influence of *ex-situ* annealing on the friction and wear performance of multi-layer $Ti_3C_2T_x$ coatings. *Appl. Mater. Today.* **2024**, *36*, 102020. DOI
39. Wang, G.; Lin, Z.; Jin, S.; Li, M.; Jing, L. Gelatin-derived honeycomb like porous carbon for high mass loading supercapacitors. *J. Energy. Storage.* **2022**, *45*, 103525. DOI
40. Mičušík, M.; Šlouf, M.; Stepura, A.; et al. Aging of 2D MXene nanoparticles in air: an XPS and TEM study. *Appl. Surf. Sci.* **2023**, *610*, 155351. DOI
41. Zhou, T.; Wu, C.; Wang, Y.; et al. Super-tough MXene-functionalized graphene sheets. *Nat. Commun.* **2020**, *11*, 2077. DOI PubMed PMC
42. Deng, Z.; Jiang, P.; Wang, Z.; Xu, L.; Yu, Z. Z.; Zhang, H. B. Scalable production of catecholamine-densified MXene coatings for electromagnetic shielding and infrared stealth. *Small* **2023**, *19*, 2304278. DOI
43. Wan, S.; Li, X.; Wang, Y.; et al. Strong sequentially bridged MXene sheets. *Proc. Natl. Acad. Sci. USA.* **2020**, *117*, 27154-61. DOI PubMed PMC
44. Usman, K. A. S.; Zhang, J.; Hegh, D. Y.; et al. Sequentially bridged $Ti_3C_2T_x$ MXene sheets for high performance applications. *Adv.*

Mater. Inter. **2021**, *8*, 2002043. DOI

45. Zhan, C.; Naguib, M.; Lukatskaya, M.; Kent, P. R. C.; Gogotsi, Y.; Jiang, D. E. Understanding the MXene pseudocapacitance. *J. Phys. Chem. Lett.* **2018**, *9*, 1223-8. DOI PubMed
46. Zhang, X.; Liu, Y.; Dong, S.; Yang, J.; Liu, X. Surface modified MXene film as flexible electrode with ultrahigh volumetric capacitance. *Electrochim. Acta.* **2019**, *294*, 233-9. DOI
47. Wu, Z.; Liu, X.; Shang, T.; et al. Reassembly of MXene hydrogels into flexible films towards compact and ultrafast supercapacitors. *Adv. Funct. Mater.* **2021**, *31*, 2102874. DOI
48. Wang, J.; Hu, Y.; Yang, B.; Wang, X.; Qin, J.; Cao, M. Mechanochemistry-induced biaxial compressive strain engineering in MXenes for boosting lithium storage kinetics. *Nano. Energy.* **2021**, *87*, 106053. DOI
49. Tang, J.; Mathis, T.; Zhong, X.; et al. Optimizing ion pathway in titanium carbide MXene for practical high-rate supercapacitor. *Adv. Energy. Mater.* **2021**, *27*, 2003025. DOI
50. Zhang, P.; Soomro, R. A.; Guan, Z.; Sun, N.; Xu, B. 3D carbon-coated MXene architectures with high and ultrafast lithium/sodium-ion storage. *Energy. Storage. Mater.* **2020**, *29*, 163-71. DOI
51. Hwang, S. K.; Patil, S. J.; Chodankar, N. R.; Huh, Y. S.; Han, Y. K. An aqueous high-performance hybrid supercapacitor with MXene and polyoxometalates electrodes. *Chem. Eng. J.* **2022**, *427*, 131854. DOI